Geophysical Journal International

Geophys. J. Int. (2010) **183,** 1470–1484 doi: 10.1111/j.1365-246X.2010.04802.x

Distribution of noise sources for seismic interferometry

Nicholas Harmon,[1] Catherine Rychert[2] and Peter Gerstoft[3]

[1] *National Oceanography Centre, University of Southampton, Southampton, UK. E-mail: n.harmon@soton.ac.uk*
[2] *University of Bristol, Bristol, UK*
[3] *Scripps Institution of Oceanography, University of California San Diego, La Jolla, CA, USA*

Accepted 2010 September 2. Received 2010 August 30; in original form 2010 January 18

SUMMARY

We demonstrate that the distribution of seismic noise sources affects the accuracy of Green's function estimates and therefore isotropic and anisotropic tomographic inversions for both velocity and attenuation. We compare three methods for estimating seismic noise source distributions and quantify the potential error in phase velocity, azimuthal anisotropy and attenuation estimates due to inhomogenous source distributions. The methods include: (1) least-squares inversion of beamformer output, (2) a least-squares inversion of year long stacked noise correlation functions assuming both a 2-D plane wave source density model and (3) a 3-D plane wave source density model.

We use vertical component data from the 190 stations of the Southern California Seismic Network and some US Array stations for 2008. The good agreement between the three models suggests the 2-D plane wave model, with the fewest number of unknown parameters, is generally sufficient to describe the noise density function for tomographic inversions. At higher frequencies, 3-D and beamforming models are required to resolve peaks in energy associated with body waves.

We illustrate and assess isotropic and azimuthally anisotropic phase velocity and attenuation uncertainties for the noise source distribution in southern California by inverting isotropic lossless synthetic Fourier transformed noise correlation function predictions from modelled 2-D source distribution. We find that the variation in phase velocity with azimuth from inhomogeneous source distribution yields up to 1 per cent apparent peak-to-peak anisotropy. We predict apparent attenuation coefficients from our lossless synthetics on the same order of magnitude as those previously reported for the region from ambient noise. Since noise source distributions are likely inhomogeneous varying regionally and with time, we recommend that noise correlation studies reporting attenuation and anisotropy incorporate source density information.

Key words: Interferometry; Surface waves and free oscillations; Seismic anisotropy; Seismic attenuation.

GJI Seismology

1 INTRODUCTION

Ambient noise surface wave tomography has improved the resolution of the crustal and upper-mantle velocity structure (Sabra *et al.* 2005; Shapiro *et al.* 2005). However, discrepancies exist between isotropic phase velocity inversions of empirical Green's functions (EGF) derived from noise correlation functions (NCF) and inversions of teleseismic data at the same periods. There is some uncertainty in both ambient noise and teleseismic data. There is a bias in the EGF data in the average phase velocities with respect to teleseismic estimates, typically <1 per cent (Yao *et al.* 2006; Yang *et al.* 2008), which after tomographic inversion of station-to-station phase into 2-D phase velocity maps leads to a bias in the phase velocities on the order of a few percent (Yao *et al.* 2006; Yang *et al.* 2008; Yao & van der Hilst 2009). An inhomogeneous source distribution in ambient noise studies is a potential cause of this bias.

Although the effect of inhomogeneous source distributions on isotropic velocity estimates is likely within the error bars of isotropic velocity studies (Bensen *et al.* 2007), it may have a more significant impact on higher-order earth models, that is, those reporting attenuation or anisotropy (e.g. Harmon *et al.* 2007; Cupillard *et al.* 2008; Matzel 2008; Prieto *et al.* 2009; Yao & van der Hilst 2009; Cupillard & Capdeville 2010). For instance, a systematic variation in phase with azimuth due to an inhomogeneous source distribution could easily be mapped into estimates of azimuthal anisotropy (Yao & van der Hilst 2009). An inhomogeneous source distribution also causes variations in the amplitude of the NCF, which must be accounted for to properly examine attenuation structure. In addition, modelling the variation in amplitude with

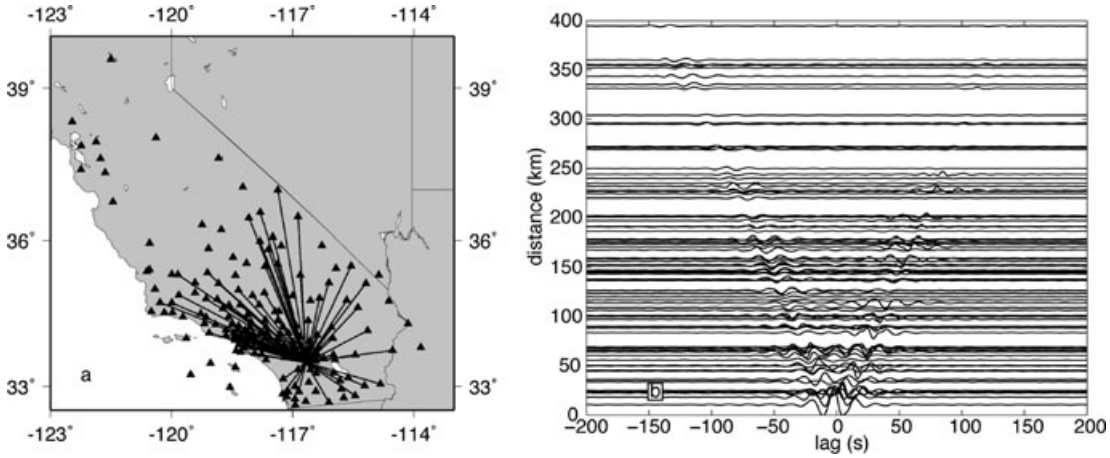

Figure 1. (a) Map of station locations (triangles) and station-to-station paths (solid) for sample record sections (b) plotted as a function of distance and lag. The sample record sections are bandpass filtered between 10–33 s.

distance of the NCF depends directly on the dimensionality of the distribution of sources (Aki & Richards 2002), that is, whether the expected amplitude falls off with station-to-station distance, s, as 1 s^{-1} in the 3-D case, where the EGF recovered is a point source, or as $1/\sqrt{s}$ in the 2-D case where the far-field EGF recovered is a line source.

The first question to consider when solving for noise source distribution is parameterization of the problem. In other words are sources confined to the surface of the earth (2-D) or distributed throughout its volume (3-D)? As shown by Harmon *et al.* (2008) and Ekström *et al.* (2009), the NCF is largely dominated by surface waves which is an azimuthally dependent, 2-D distribution of sources confined to the surface of the Earth. This has also been explored analytically (Nakahara 2006; Harmon *et al.* 2008; Tsai 2009). However, in the higher frequencies of the secondary microseism band, there may be noise sources that contribute to the EGF that travel across the seismic arrays at all incidence angles caused by scattering or body waves (Gerstoft *et al.* 2008). In other words, in the microseism band there may be a 3-D or azimuthal and incidence angle-dependent distribution of sources.

In this paper, we develop a method to estimate the distribution of noise sources, assuming either 2-D or 3-D source distribution, from the NCF and compare these methods to results from a noise source distribution obtained by beamforming on the NCF. Using data from the Southern California Seismic Network and some of the USArray stations (which hereafter referred to as the extended SCSN) shown in Fig. 1. With these observations we demonstrate to first-order the year long average distribution of noise sources at 7–25-s period is consistent with an azimuthally dependent 2-D distribution of noise, with the coherent sources travelling mostly as surface waves from west to east. A detailed analysis of the dominant arrivals versus frequency and time-of-year can be found in Gerstoft & Tanimoto (2007). We demonstrate how to analytically calculate and correct for the effects of inhomogeneous noise distribution on the amplitude and phase of the NCF for all three methods. Using the best-fit model of the observed inhomogeneous noise field in the extended SCSN and the model's predicted synthetic NCF, we also evaluate the magnitude of the errors caused by the assumption of an isotropic noise field that could contribute to 1-D anisotropy and attenuation results.

2 METHODS

We model the frequency domain NCF (FNCF) for both a 2-D and 3-D plane wave source density functions using analytical expressions after Aki (1957) and Cox (1973). We use these expressions to set up the linear inverse problem, inverting the FNCF for the source density function. In addition, we detail a method for converting beamformer output to a 2-D amplitude density function. From these models we also derive expressions to predict the phase delay for a given inhomogeneous source distribution for any station-to-station path in an array. This phase delay can then be used to correct phase velocities used in tomographic inversions for source effects.

2.1 2-D source model

Following Cox (1973), the 2-D noise field is described by a superposition of uncorrelated plane waves from all azimuths with a normalized amplitude density function, A(θ), of plane wave azimuth, θ. We note that our plane wave formulation is an alternative to the stationary phase constructions used in other studies (Snieder 2004; Halliday & Curtis 2008).

The frequency domain correlation function (FNCF or R in eqs 1–4) for two stations separated by distance *s,* station to station azimuth ζ and phase velocity c can be obtained by integrating the phase delay of a plane wave between the stations over all azimuths weighted by the normalized amplitude density function of A(θ):

$$R(\omega, s/\mathrm{c}(\omega), \zeta) = \frac{1}{2\pi}\int_0^{2\pi} A(\theta)\exp\left(i\frac{\omega s}{\mathrm{c}(\omega)}\cos(\theta-\zeta)\right)\mathrm{d}\theta. \quad (1)$$

Expanding A(θ) in a Fourier series, the integral is recast as an infinite series (Cox 1973):

$$R(\omega, s/\mathrm{c}(\omega), \zeta) = \sum_{m=0}^{\infty} i^m \varepsilon_m J_m\left(\frac{\omega s}{\mathrm{c}(\omega)}\right)[a_m(\omega)\cos(m\zeta) + b_m(\omega)\sin(m\zeta)]$$
$$= a_0 J_0\left(\frac{\omega s}{\mathrm{c}(\omega)}\right) + 2\sum_{m=1}^{\infty} i^m J_m\left(\frac{\omega s}{\mathrm{c}(\omega)}\right)[a_m(\omega)\cos(m\zeta) + b_m(\omega)\sin(m\zeta)], \quad (2)$$

where ε is 1 when $m = 0$ and 2 otherwise and a_m and b_m are the Fourier coefficients of the amplitude density function. J_m is the Bessel function of the first kind. Note that for a uniform amplitude density, $R(\omega) \sim J_0(\omega \mathrm{s}/\mathrm{c})$.

For a given noise field, described by its Fourier coefficients a_m and b_m, synthetic FNCFs can be computed for all station pairs in the array using eq. (2). Conversely for observed FNCFs for all station pairs in an array, eq. (2) can be used to linearly invert for the parameters a_m and b_m, using a truncated series of a small number of Fourier coefficients, see Section 2.7.

2.2 3-D source model

For a 3-D distribution of plane waves the integral form of the FNCF is given by Eq. (43) in Cox (1973):

$$R(\omega, s/c(\omega), \zeta, \gamma) = \frac{1}{4\pi}\int_0^{\pi}\int_0^{2\pi} A(\theta, \phi)\sin(\phi)\exp\left(i\frac{\omega s}{c(\omega)}\sin(\phi)\sin(\gamma)\cos(\theta - \zeta) + \cos(\phi)\cos(\gamma)\right)\mathrm{d}\theta\,\mathrm{d}\phi, \quad (3)$$

where ϕ, is the incidence angle of the plane wave from the z-axis in spherical coordinates and γ is the station-to-station angle relative to the z-axis. Similar to the 2-D case the FNCF is rewritten as a summation over the spherical harmonic expansion of A(θ,ϕ) (Cox 1973):

$$R(\omega, s/\mathrm{c}(\omega), \zeta, \gamma) = \sum_{n=0}^{\infty}\sum_{m=0}^{n} i^n j_n\left(\frac{\omega s}{\mathrm{c}(\omega)}\right)P_n^m(\cos(\gamma))\left[a_n^m(\omega)\cos(m\zeta) + b_n^m(\omega)\sin(m\zeta)\right]$$
$$= a_0^0 j_0\left(\frac{\omega s}{\mathrm{c}(\omega)}\right) + \sum_{n=1}^{\infty}\sum_{m=0}^{n} i^n j_n\left(\frac{\omega s}{\mathrm{c}(\omega)}\right)P_n^m(\cos(\gamma))\left[a_n^m(\omega)\cos(m\zeta) + b_n^m(\omega)\sin(m\zeta)\right], \quad (4)$$

where γ is the station-to-station angle from the z-axis in the spherical harmonic expansion, j_n is the spherical Bessel function and P_n^m is the associated Legendre polynomial of order m, degree n and a_n^m and b_n^m are the spherical harmonic coefficients of the amplitude density function A(θ,φ). For uniform A(θ,φ), the integral of eq. 3 is proportional to the sinc function, $j_0\,(\omega \mathrm{s}/\mathrm{c}(\omega)) = \sin(\omega \mathrm{s}/\mathrm{c}(\omega))/(\omega \mathrm{s}/\mathrm{c}(\omega))$. Again, the advantage of this parameterization is that it can be used to directly linearly invert the NCF for the parameters a_n^m and b_n^m, with a truncated series of a small number of parameters, see Section 2.7.

Assuming the stations lie on the surface of a flat Earth, therefore $\gamma = 90^\circ$, eq. (4) is simplified:

$$R(\omega, s/\mathrm{c}(\omega), \zeta, \gamma) = a_0^0 j_0\left(\frac{\omega s}{\mathrm{c}(\omega)}\right) + \sum_{n=1}^{\infty}\sum_{m=0}^{n} i^n j_n\left(\frac{\omega \mathrm{s}}{\mathrm{c}(\omega)}\right)P_n^m(0)\left[a_n^m(\omega)\cos(m\zeta) + b_n^m(\omega)\sin(m\zeta)\right], \quad (5)$$

where $m + n$ must be even. The assumed station geometry (stations lying in a plane) does not prevent us from detecting vertically incident plane waves, but we cannot differentiate between energy coming from above or below the plane. We assume all energy comes from the earth beneath the stations. The reduced resolution due to the station geometry and resulting truncation of the series means that only the longest wavelength features of the vertically incident wavefield will be apparent.

2.3 Implications of source models

This theory has two important ramifications: (1) These models predict that the amplitude decay for the 2-D model (J_0) in its asymptotic form ($\sqrt{(}2\mathrm{c}(\omega)/\pi\omega s)\cos(\omega s/\mathrm{c}(\omega)–\pi/4)$) is proportional to $1/\sqrt{\mathrm{s}}$, while for the sinc function, the amplitude is proportional to 1 s^{-1}. 2) The proper way to extract the Green's function is based on the dimensionality of sources, that is, in the 3-D case a time derivative of the NCF is needed or in the 2-D case a Hilbert transform with a $\pi/4$ correction is needed to estimate phase velocity for tomography (Nakahara, 2006; Sanchez-Sesma & Campillo 2006; Harmon *et al.* 2007; Harmon *et al.* 2008; Tsai 2009),

To apply these equations to real data we use the average phase velocity between each station-to-station pair (detailed in Section 2.5). We assume (1) The error in phase velocity is small. (2) All station pairs have the same source distribution on average. (3) The source density function is relatively smooth in azimuth. (4) The FNCFs for different station pairs are recording data for approximately equivalent times. We assess these assumptions in subsequent sections.

2.4 NCF calculation

We used the long period vertical records, sampled at 1 Hz from 190 stations of the SCSN array and some of the USArray stations in the Western US (Fig. 1) for Jan 1–Dec 31, 2008 (366 d). After removing the instrument response from the data, we bandpass filtered (0.02–0.30 Hz) and normalized the time-series using the envelope. Using a 2^{18} point (>2× length of one day time-series to prevent the signal from wrapping around), zero padded fast Fourier transform (FFT) the signals were whitened by Fourier coefficient normalization within the bandpass limits. For each frequency bin and for all station pairs, the NCF is computed and stacked for all possible days for all station pairs.

This processing makes the amplitude of the NCF comparable between station pairs because only the phase information is kept, that is, the maximum amplitude at a given frequency is 1 for any one-day NCF. Theoretically, NCFs with the same number of days in the stack have the same maximum amplitude, making comparison between NCFs straightforward. We present spectral data from NCF that have > 330 d stacked and have a station-to-station separation > 10 km. We normalized the real and imaginary components of the NCF spectra by the number of days in the stack. We use a cosine taper window on the NCF with a 20 s fall-off each end of a 1600 s window centred on zero lag and Fourier transform the data.

Comparison of data between FNCF with different numbers of stacked days implicitly assumes that the variation of the noise source distribution between the FNCF with different numbers of stacked days was small. We assume that the $366–330 = 36$ d difference will contribute to the scatter in the data about the model, but will not be sufficient to obscure the overall picture. In fact, 43 per cent of the data have 366 d and 70 per cent have over 350 d. The difference between the noise fields for station pairs should average out because the days missing for many stations were scattered intermittently throughout the year. We repeated our experiments using only stations pairs with the maximum number of days (366) and found the model coefficients were within 95 per cent confidence limits of the 330 d model estimate.

2.5 Phase velocity estimation

Here the phase velocity for a given station-to-station path is estimated from the causal, symmetric component of the NCF; in other words only the real part of the FNCF is used. This causal, symmetric component is derived by summing the causal and time-reversed acausal NCF in the time domain. In the frequency domain, this is equivalent to replacing the imaginary component of the FNCF with the negative Hilbert transform of the real component of the FNCF with respect to frequency (Oppenheim & Schafer 1975; Bendat & Piersol 2000). This frequency domain relationship will allow us to use eq. 2 and 4 to analytically determine and approximate the phase delay caused by inhomogeneous source distribution in Section 2.8 by processing the synthetic NCF in the same manner we process our data.

To estimate the average surface wave phase velocity (c in eqs 1–4) for each station pair NCF we use the method of Harmon *et al.* (2008). In this method, we first calculate the causal, symmetric component of the NCF as described above. We then determine the phase of the signal, ϑ, which we use to calculate the phase velocity, $\mathrm{c} = \mathrm{s}\omega/(\vartheta + 2\pi n - \delta)$, where n is the number of spatial cycles and δ is the phase shift due to the NCF source effects relative to a plane wave. The phase shift is assumed to be $-\pi/4$ for a homogeneous source distribution (Yao *et al.* 2006; Bensen *et al.* 2007; Harmon *et al.* 2008; Lin *et al.* 2008). The cycle ambiguity was removed by matching the average phase velocity for the extended SCSN at 25 s (Yang & Forsyth 2006). At the longest periods 25–40 s useable for our purposes, the average phase velocity from ambient noise is within <1 per cent from the dispersion curve of Yang & Forsyth (2006) derived from earthquakes using the two-plane wave approximation Rayleigh wave tomography method. Our phase velocities are used to project the data into distance/wavelength $[\omega s/(\mathrm{c}(\omega)2\pi)]$ domain, assuming that our initial estimate is within a few per cent of the effective velocity. By employing the station-to-station phase velocity we can account for the variations in wavelength caused by variations in velocity when solving for 2-D source distribution.

For the 3-D source model and the beamforming model the velocity of vertically incident body waves will be different than the surface wave phase velocity. However, when inverting for 3-D source density functions using eq. 4, we assume $\mathrm{c}(\omega)$ is the apparent surface wave phase velocity between each station pair. This causes a systematic error in the 3-D source estimation, specifically, mis-location of the amplitude density in incidence angle, that is, there will be a trade-off between incidence angle of a plane wave in the horizontal slowness term in eq. 3 $[\sin(\phi)/\mathrm{c}(\omega)]$. The beamforming method does not depend directly on the phase velocities determined here, but assumes a uniform phase velocity. Therefore, the beamforming method does not take into account variations in earth structure and may leak beamformer power into adjacent slowness and azimuths as different parts of the array become coherent near the true local slowness. The incidence angle ambiguity in both models could be resolved by assuming velocities appropriate for body waves but is beyond the focus of this paper.

2.6 Beamforming

Beamforming was performed similar to Gerstoft & Tanimoto (2007) using a 2^{12} sample Fourier transform of the >330 d stacked NCF. The main difference in the approach applied here is that the FNCF is a nearly year long ensemble average of noise cross correlations instead of a 1.5 hr ensemble average of frequency domain cross correlations of clipped noise signals used in Gerstoft & Tanimoto (2007), though we expect that stacking the beamformer output from shorter time-series would produce similar results.

At each frequency, the Fourier transformed NCF for each station-to-station pair can be used to form a cross spectral density matrix $\mathbf{C}(\omega)$ of the array formed by the 190 stations. The diagonal of $\mathbf{C}(\omega)$ corresponds to the time domain autocorrelation for each station and the off diagonal elements, upper and lower triangles of $\mathbf{C}(\omega)$, corresponds to the station-to-station cross correlations, with the row and column determining the cross correlation corresponding to the station autocorrelations on the respective diagonal. We set the lower triangle and diagonal of $\mathbf{C}(\omega)$ to zero in the present study (e.g. Westwood 1992; Yardibi *et al.* 2008). The plane wave response for the seismic array is given by $\mathbf{p}(\omega, \mathrm{c}, \theta, \boldsymbol{r}) = \exp(\mathrm{i}\omega(\mathbf{re})/\mathrm{c})$, where $\boldsymbol{r}$ describes the coordinates of the array relative to the mean coordinates and $\mathbf{e}$ contains the directional cosines of the plane wave. The beamformer output in our modified approach is given by: $\mathrm{b}(\omega, \mathrm{c}, \theta) = 2\,\mathrm{Re}[\mathbf{p}(\omega, \mathrm{c}, \theta)^{\mathrm{H}}\mathbf{C}(\omega)\mathbf{p}(\omega, \mathrm{c}, \theta)]$, where H indicates complex conjugate transpose. Adding the contribution from the diagonal $\mathbf{C}(\omega)$, which is always real, yields the beamformer output in Gerstoft & Tanimoto (2007) and Yardibi *et al.* (2008).

We searched for the maximum beamformer output, corresponding to the best-fitting plane wave, over slowness (1/c) from 0–0.40 s km^{-1} every 0.01 s km^{-1} and every 1° from 0–360° azimuth.

2.7 Inverting FNCF for source density functions

Assuming a 2-D source density function, eq. (2), we invert the real and imaginary components of the normalized FNCF from all station-to-station pairs at a given frequency for the Fourier series expansion coefficients (a_m and b_m) which are assumed to be identical for all stations. We use the observed phase velocity and the station-to-station azimuth ζ and distance s to calculate the matrix of partial derivatives of R with respect to a_m and b_m, **G**, as a function of $\omega s/\mathrm{c}(\omega)$ for each station pair. Thus **G** will have dimension *Npair* by $1 + 2K$, with *Npair* being number of station pairs and K the order of Fourier coefficients used in the expansion. We use a least-squares solution of the form:

$$\mathbf{M} = (\mathbf{G}^T\mathbf{G})^{-1}\mathbf{G}^T\mathbf{d}, \tag{6}$$

where **M** is the model vector of a_m and b_m, and **d** is the complex-valued FNCF for all *Npair* station pairs at a given frequency. We calculate the synthetic FNCF for the 2-D models after inverting for the best-fitting coefficients by calculating the best-fitting forward model using eq. (2) with the best estimates for average velocity between each station pair. The derivatives of eq. (2) with respect to a_m and b_n form a well-conditioned inverse of $(\mathbf{G}^T\mathbf{G})$ and no regularization is required.

Similarly for the 3-D model, using eq. (5), we take the derivatives of R with respect to a_n^m and b_n^m to form our matrix of partial derivatives. Again, no damping is required, because the partial derivatives of eq. (4) yield a well-conditioned inverse.

To transform the beamformer output to a source density function, the effects of the array geometry must be deconvolved from the beamformer output. The extended SCSN has a greater aperture in a roughly NW–SE direction and will therefore have greater sensitivity and yield higher beamformer output in those directions. A simple way to address this problem is to recast beamforming in terms of a linear inverse problem in which the forward model is described either by eqs (1) or (3) where we solve for A. Taking the simpler 2-D case and numerically approximating eq. (1) using the rectangle rule for numerical integration, **G** in this case becomes the matrix of partial derivatives of R with respect to $\mathrm{A}(\theta_\mathrm{i})$, $\mathrm{d}\theta = 1°$, where subscripts i refers to the column and j refers to the row of the matrix:

$$G_{i,j}(s_j, \omega, \mathrm{c}(\omega), \theta_i) = \frac{1}{2\pi}\exp\left(i\frac{\omega s_j}{\mathrm{c}(\omega)}\cos(\theta_i - \zeta)\right)\,\mathrm{d}\theta \tag{7}$$

thus **G** will have dimension *Npair* by 360.

Inspection of the linear least-squares solution given in eq. (6), assuming **d** is the complex-valued vector of the FNCF, the real component of $\mathbf{G}^T\mathbf{d}$ vector is related to the beamformer output as we defined it in Section 2.6 at all azimuths at a given slowness (1/c) and frequency. The array response, or amplitude leakage across all azimuths for an input plane wave at a given θ_i is then given by the real component of $\mathbf{G}^T\mathbf{G}$. The deconvolution operator for the array response is given $(\mathbf{G}^T\mathbf{G})^{-1}$ and can be applied to the beamformer output at a given slowness.

In practice $\mathbf{G}^T\mathbf{G}$ is ill-conditioned and requires some regularization for stable inversion. We introduce a smoothing operator into our array response deconvolution operator $(\mathbf{G}^T\mathbf{G}+\mathbf{S})^{-1}$ where **S**:

$$\mathbf{S} = \lambda\begin{bmatrix} 2 & -1 & 0 & 0 & 0 & \cdots & -1 \\ -1 & 2 & -1 & 0 & 0 & \cdots & 0 \\ 0 & -1 & 2 & -1 & 0 & \cdots & 0 \\ \vdots & & & \ddots & & & \vdots \\ 0 & \cdots & 0 & -1 & 2 & -1 & 0 \\ 0 & \cdots & 0 & 0 & -1 & 2 & -1 \\ -1 & \cdots & 0 & 0 & 0 & 2 & -1 \end{bmatrix}. \tag{8}$$

We choose λ such that the trace of the resolution matrix of our deconvolution operator given by $(\mathbf{G}^T\mathbf{G}+\mathbf{S})^{-1}\mathbf{G}^T\mathbf{G}$ is roughly the same as the number of 2-D model parameters to make comparison between the methods more straightforward. If the FNCF is inverted directly this approach has similarities to Yao & van der Hilst (2009). The deconvolution operator for the full beamformer output can be constructed for the 3-D model given in eq. (3) and could yield a more accurate estimate of the 3-D source density function if accurate body wave velocity information is included.

To examine surface wave source densities from the beamformer output we average over surface wave slownesses within ± 0.01 s km^{-1} from the slowness corresponding to the maximum beamformer output. We then apply the array response deconvolution operator to the average beamformer output to yield a 2-D estimate of the source density function. We refer to this in the text as the 2-D beamforming model (2-D BM).

2.8 Correcting phase velocity estimates for inhomogeneous sources

Knowing the source density function, we can calculate the phase delay caused by inhomogeneous source distribution and then correct the phase velocity estimate for each station-to-station path for this effect. Specifically, to determine the phase shift, δ, relative to a plane wave

caused by inhomogeneous source distribution we perform the same operations on the synthetic FNCF as on the observed data (see Section 2.5). We first calculate the frequency domain causal, symmetric component of the synthetic FNCF by equating the imaginary component to minus the Hilbert transform of the real component. We calculate the Hilbert transform of the real component of the synthetic FNCF with respect to $\omega s/\mathrm{c}(\omega)$, with only the range s varying (ω and c are constant). This can be accomplished numerically on the FNCF or analytically by summing the Hilbert transform of the real components of eqs (2) and (4) using the fitted coefficients, a, and b. We then calculate the phase of the causal symmetric component and subtract the plane wave phase ($\omega s/\mathrm{c}(\omega)$):

$$\delta(\omega, s/\mathrm{c}(\omega), \zeta) = \angle\left(\mathrm{Re}\{R(\omega, s/\mathrm{c}(\omega), \zeta)\} - i\boldsymbol{H}\left\{\mathrm{Re}\{R(\omega, s/\mathrm{c}(\omega), \zeta)\}\right\}\right) - \left(\frac{\omega s}{\mathrm{c}(\omega)}\right), \tag{9}$$

where $\boldsymbol{H}$ indicates the Hilbert transform and $\angle$ is the unwrapped angle of the causal, symmetric component. This phase difference is the required phase correction for the given source distribution.

Determining the phase shift of the causal symmetric component relative to a plane wave for the 2-D model is therefore given by summation over the even terms of m:

$$\delta(\omega, s/\mathrm{c}(\omega), \zeta) = \angle\left(\sum_{m=0}^{\infty} i^m \varepsilon_m \left[J_m\left(\frac{\omega s}{\mathrm{c}(\omega)}\right) - i\boldsymbol{H}\left\{J_m\left(\frac{\omega s}{\mathrm{c}(\omega)}\right)\right\}\right]\left[a_m(\omega)\cos(m\zeta) + b_m(\omega)\sin(m\zeta)\right]\right) - \left(\frac{\omega s}{\mathrm{c}(\omega)}\right). \tag{10}$$

For the zero-order term, the Hilbert transform of J_0 is a zero-order Struve function and the phase shift oscillates asymptotically around $-\pi/4$ (Harmon *et al.* 2007; Harmon *et al.* 2008; Tsai 2009). This oscillation is not observed in practice because the NCF is usually windowed in the time domain, which will smooth the phase across frequency and in our case across distance, effectively averaging out the oscillation. To account for the smoothing effects of windowing, we numerically calculate the Hilbert transforms and the phase shift and then apply a moving average filter to the phase shift to cancel out the oscillation. We choose the width of the filter to average over 1 wavelength to yield the slowly varying average value, which approximates the smoothing of our windowing well (phase error <0.1 per cent) at >1 wavelength. Therefore, only phase shift for distance/wavelength >1 is discussed.

Similarly in 3-D, the phase shift is given by summation over the even terms of n with the Hilbert transform of the spherical Bessel function:

$$\delta(\omega, s/\mathrm{c}(\omega), \zeta) = \angle\left(\sum_{n=0}^{\infty}\sum_{m=0}^{n} i^n \left(j_n\left(\frac{\omega s}{\mathrm{c}(\omega)}\right) - i\boldsymbol{H}\left\{j_n\left(\frac{\omega s}{\mathrm{c}(\omega)}\right)\right\}\right) P_n^m(0)\left[a_n^m(\omega)\cos(m\zeta) + b_n^m(\omega)\sin(m\zeta)\right]\right) - \left(\frac{\omega s}{\mathrm{c}(\omega)}\right). \tag{11}$$

For the zero-order model, $\boldsymbol{H}\{j_0(x)\} = 1/x + y_0(x)$, which will yield an oscillatory phase shift. As for the 2-D case, we present the smoothed phase shift from the numerical estimate of the Hilbert transform.

To highlight the azimuthal variation in phase shift, in Sections 3.2 and 3.3, we present $\delta + \pi/4$ versus cycles, which is the phase correction needed beyond the correction for a far-field isotropic 2-D source distribution ($-\pi/4$). For a 2-D homogeneous source distribution this should have roughly zero mean, except at small distances (<1 wavelength) where the far field approximation breaks down. This allows us to identify station-to-station azimuths and distances where the standard $-\pi/4$ correction does not apply.

3 INVESTIGATION OF SOURCE DIMENSIONALITY (2-D VS. 3-D)

3.1 NCF as a function of station-to-station distance/wavelength

Here we examine whether the observed noise source distribution is 2-D (J_0, Bessel function) or 3-D (j_0, sinc). To accomplish this, we project the real component of the Fourier transformed NCF data into distance/wavelength (dimensionless wavenumber or number of spatial cycles of the wave) domain (Fig. 2). This domain is preferable to station-to-station distance because it accounts for velocity variation (see Section 2.5). We plot all station-to-station pairs that fit our selection criteria, or 12485 data (grey dots in Fig. 2). As expected the data vary sinusoidally with respect to dimensionless wavenumber. We average the real component of the FNCF in distance/wavelength bins with a spacing of 0.1 and compare our data average to an RMS amplitude normalized J_0 and sinc functions with respect to distance/wavelength (Fig. 2), which are equivalent to the zero-order/degree coefficients in the modelling.

The phase and amplitude decay of the binned average of all data (black dashed line in Fig. 2) with distance are best matched by a Bessel function of the first kind, J_0, (green line in Fig. 2) rather than a sinc function (red line in Fig. 2) at the longer periods. For example, at 25-s period the averaged data are correlated with the Bessel function at 0.95, while they are correlated at only 0.75 with the sinc. This is also true at longer periods: at 28 s, correlation coefficients of 0.94 versus 0.76 and at 33 s correlation coefficients of 0.90 versus 0.81. The correlation coefficient between J_0 and sinc function models is 0.78 for the number of wavelengths used here. Our choice of phase velocity does impact the phase of data and a different phase velocity will change the correlation with J_0. However, the phase velocity has no impact on the amplitude decay with distance, which is proportional to $1/\sqrt{s}$, independently supporting the Bessel function model.

In the microseism band at 5 s (Fig. 2a) neither the J_0 nor the sinc function fit the data well, with correlation coefficients if 0.60 and 0.22, respectively. This is an indication that the source function is more complicated than either zero-order/degree models would predict and that the earth's structure may be very heterogeneous. We will show in Section 3.4 there is a strong non-uniform body wave or scattered surface wave component in the beamformer output and 3-D models at 5-s period.

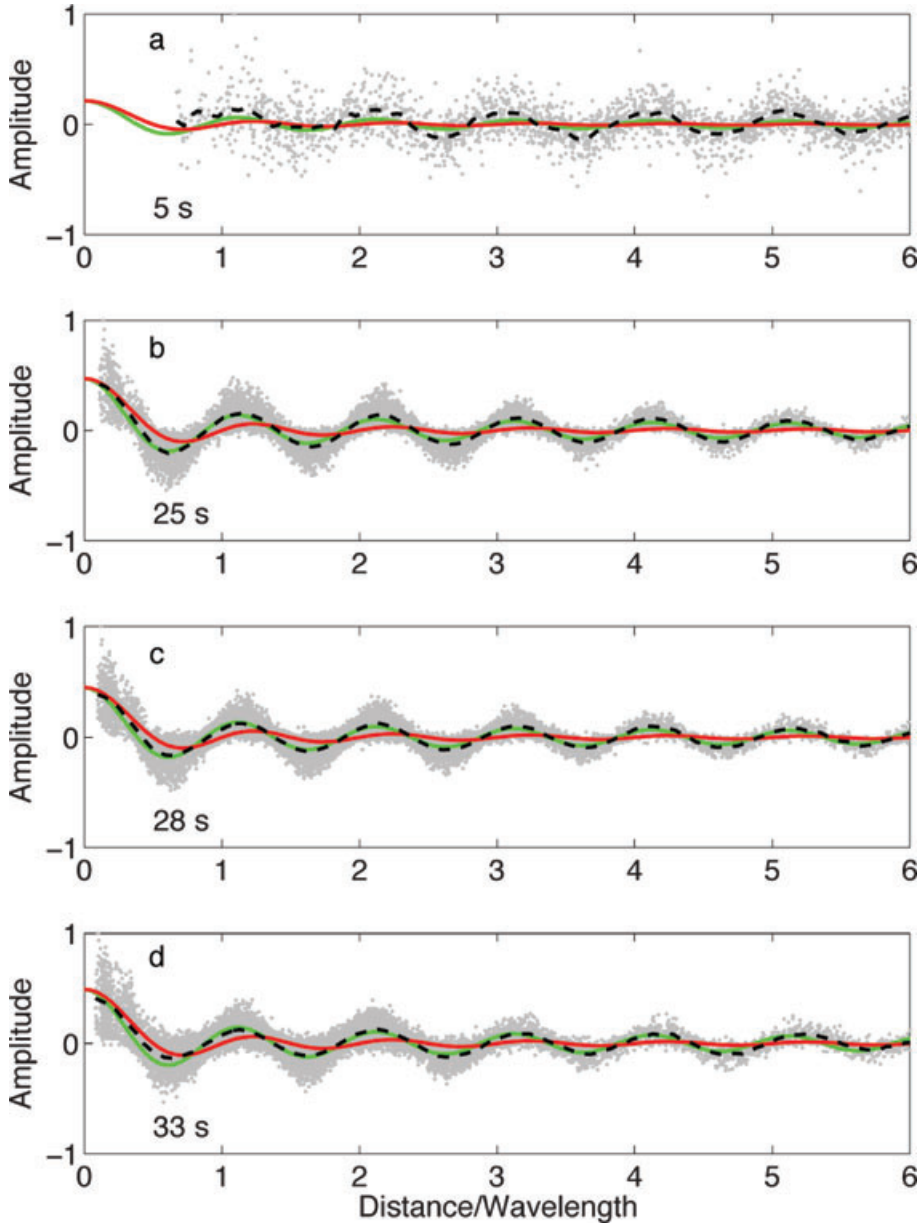

Figure 2. Real component of the Fourier transformed NCF (grey dots, normalized so the largest value is 1) as a function of dimensionless wavenumber (distance/wavelength) for 5 (a), 25 (b), 28 (c) and 33 (d) s period. The binned average of the data (black dashed line), $J_0(\omega s/c)$ (green) and sinc function (red) is also shown for each period.

3.2 NCF as a function of azimuth and station-to-station distance/wavelength

To investigate azimuthal variations in the FNCF data, we project and average the real and imaginary components of the FNCF for both azimuthal directions of all station pairs into 0.1 distance/wavelength and 1° azimuth bins. For this binning, we note that time reversal of the NCF, or switching azimuthal direction, is equivalent to complex conjugation of the FNCF. This projection allows us to visualize the variation in amplitude with azimuth in the FNCF caused by the noise source distribution. We consider a single period, 25 s (Figs 3a and b) and observe a coherent pattern, rather than random noise, suggesting that the entire array is seeing the same noise sources. The data vary cyclically with increasing distance/wavelength for all azimuths for both the real and imaginary components as observed in Fig. 2. There is a significant imaginary component to the data, an indication of asymmetry of the source distribution. In both the real and imaginary components, we observe a systematic variation in amplitude with azimuth. The amplitudes of the real and imaginary components are larger in a roughly 290° azimuth, with the imaginary component showing 180° asymmetry about the origin. The scatter at a given distance/wavelength in Fig. 2 is caused by this azimuthal variation.

In Fig. 3(c) we plot the azimuth and distance/wavelength binned and averaged phase shift, $\delta + \pi/4$, in cycles of the observed causal, symmetric NCF, to highlight the azimuthal variation in phase shift caused by source heterogeneity at 25 s. A negative region indicates an apparent phase velocity that is faster than the assumed average velocity and a positive region indicates an apparent phase velocity that is

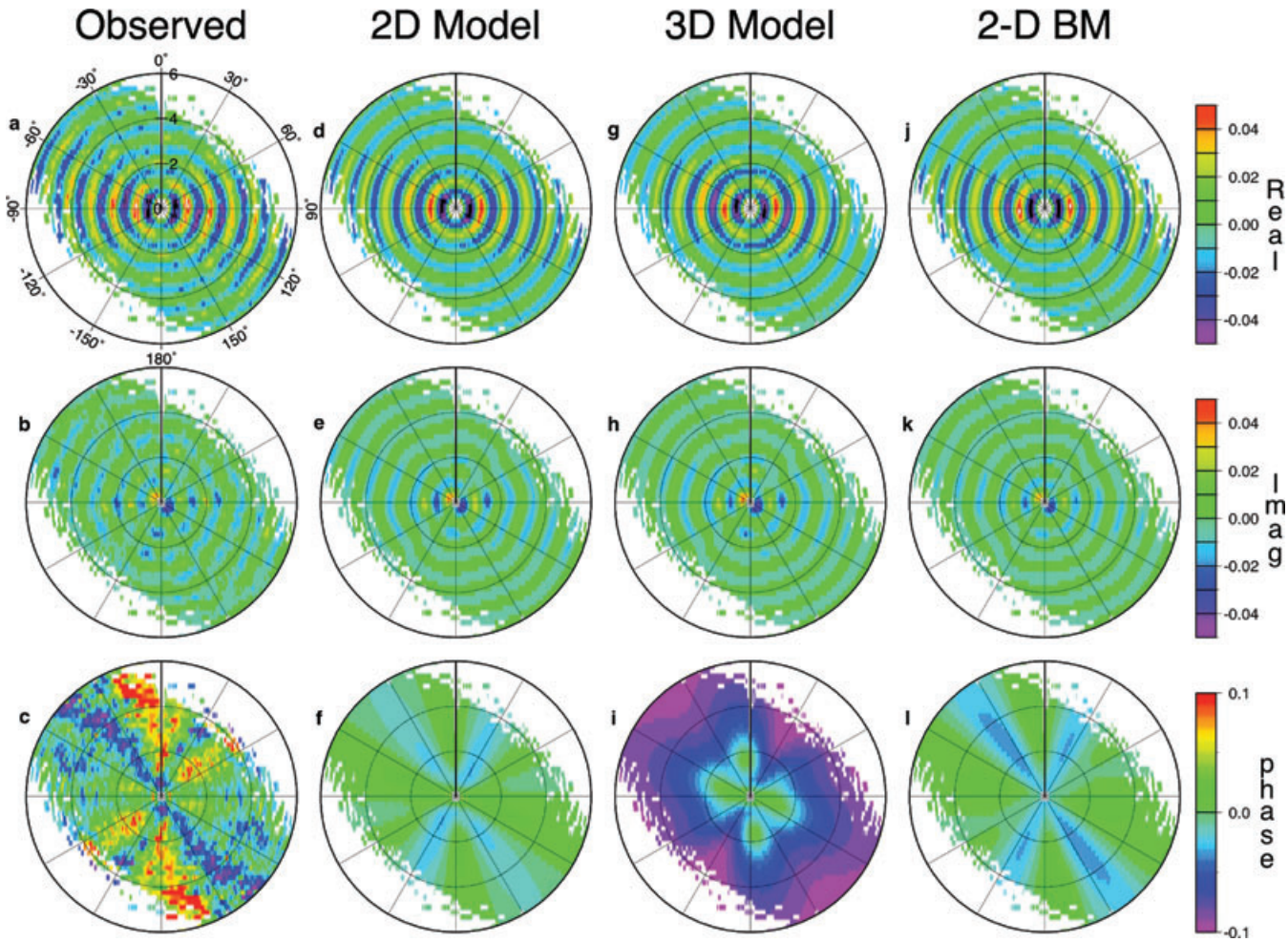

Figure 3. FNCF real (top row), imaginary (middle row) components and phase shift ($\delta+\pi/4$) in cycles (bottom row) of the observed (column 1 a,b,c), 2-D model (column 2 d,e,f), 3-D model (column 3 g,h,i) and 2-D beamforming (2-D BM, column 4 j,k,l) at a period of 25 s. The radial axis is distance/wavelength and azimuth is the angular axis.

slower than the average velocity. We see no oscillation in the phase shift with respect to distance/wavelength, likely due to the effects of windowing of the time-series. The dominant pattern with respect to azimuth in the observed phase shift is a rough 180° azimuthal symmetry, with negative bands extending radially with an azimuth of 150° (−30°) and 22° (−158°). In between there are regions of positive phase shift. There is some speckle in the phase shift likely caused by scattering and velocity variations across the region (e.g. Tsai 2009; Yao & van der Hilst 2009). However, the observed overall symmetry is predicted by eqs (10) and (11) for inhomogeneous sources, which have only 2θ, 4θ, etc. azimuthal variation, suggesting to first-order that our assumptions are reasonable at 25-s period and we proceed applying eqs (2) and (4) to the data.

3.3 Higher-order source models: forward models from best-fitting source distributions versus observations

Here we compare the FNCF observations in azimuth and distance/wavelength space to the synthetic FNCF and phase shift ($\delta + \pi/4$ in cycles) from the best-fitting 2-D (Figs 3d–f), 3-D (Figs 3g–i), and 2-D BM (Figs 3j–l). We calculate the synthetic FNCF from our best-fitting amplitude density functions for the 2-D and 3-D source distribution models for an example period, 25 s (Figs 3d, e, g, h). In other words, we calculate the forward models shown in Fig. 3 by using the best-fitting model coefficients a and b and $m = 8$ (2-D) and $n = 8$ (3-D) in equations 2 and 4 (see Section 3.4, Fig. 4 and Tables 1 and 2 for description of the best-fitting amplitude densities). The number of parameters was chosen so that the azimuthal resolution of the source density models and fit to the data was approximately the same. We assume a homogeneous isotropic phase velocity (3.65 km s^{-1}) across the region. For the 2-D BM synthetic FNCF (Figs 3j and k), we numerically integrate eq. 1, using the best-fitting 2-D amplitude density function again assuming the same homogeneous isotropic phase velocity across the region. We choose λ in eq. 8 so that the resolution of 2-D BM and the 2-D and 3-D models are approximately the same (∼45° resolution in azimuth). The predicted phase shifts of the 2-D and 3-D models (Figs 3f and i) and the 2-D BM (Fig. 3l) were calculated as described in Section 2.8 from the real component of the synthetic FNCF.

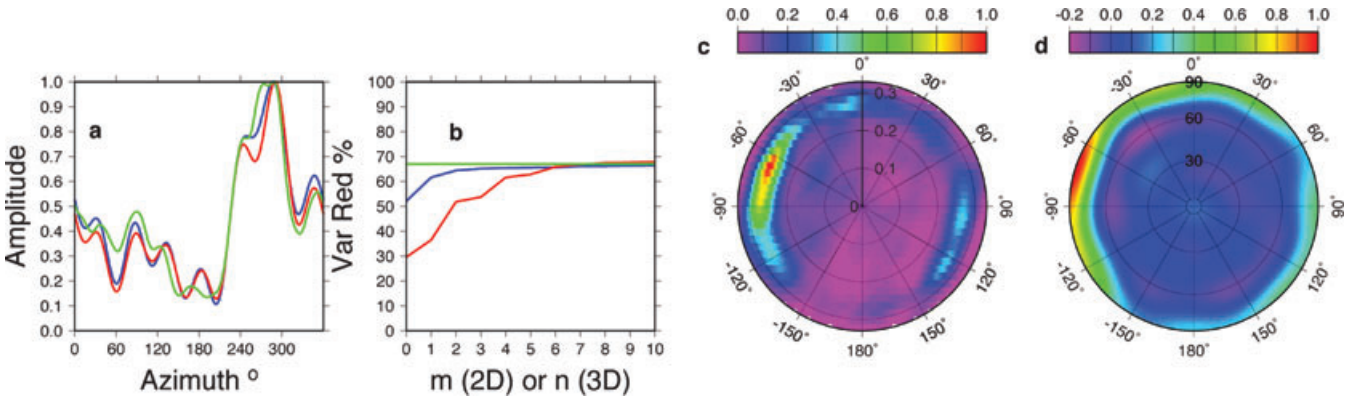

Figure 4. Comparison of the three methods at 25-s period. (a) 2-D (blue), 3-D (red) and 2-D beamforming (green) equivalent 2-D Source density functions, normalized to 1. (b) Variance reduction of the data (R^2) for the 2-D (blue), 3-D (red) and 2-D beamforming (green) source density functions. (c) Beamformer output azimuth versus slowness and (d) 3-D model density function azimuth versus incidence angle.

Table 1. 2-D noise model power at 25-s period.

m	
0	0.113
1	0.034
2	0.020
3	0.011
4	0.006
5	0.003
6	0.004
7	0.011
8	0.002

The synthetics derived from the three source distribution models match the observed FNCF well (Fig. 3). This is true for both the real and imaginary components and particularly true from distance/wavelengths 0–3 where the amplitudes are highest. Specifically, all three models have a real component with similar magnitude and pattern (higher amplitudes roughly in the E–W direction). The three models also predict imaginary components with the highest amplitudes in a roughly E–W direction with similar but slightly lower amplitudes than the observations.

The phase shift of the 2-D and 2-D BM matches the observed phase shift, but the 3-D model begins to shift in phase relative to the observations at wavenumbers >3. Comparison of the phase shift $\delta+\pi/4$, in cycles between the three models (Figs 3f, i, l) and the observed data (Fig. 3c) shows that all three models pick up the reduced phase shift at $\sim -30^\circ$ and 22° azimuth. The magnitude of the negative phase is better represented in the 2-D model and the 2-D BM. The 3-D model systematically under predicts the phase shift at distance/wavelength >3, approaching a $\delta+\pi/4$ of $-\pi/4$ (0.125 cycles) in Fig. 3(i). At these larger distances, the 3-D model is approaching the phase shift predicted for a far field 3-D distribution ($\delta = -\pi/2$ or -0.25 cycles) relative to a plane wave.

The visual agreement of the pattern of the $\delta+\pi/4$ between the observed phase shift and the 2-D beamforming and 2-D models suggests a 2-D model is the most appropriate model at this period. However, there are significant differences in the predicted phase between the two models as described above. Specifically, the 2-D BM has a larger magnitude phase shift (-0.06 to 0.03 cycles relative to the expected 0.125 cycle shift required for a homogeneous distribution) at 22° and -30° azimuths relative to the 2-D model (-0.03 to 0.02 cycles relative to 0.125 cycles) and appears to match the observed phase better. If the 2-D model were calculated using $m > 8$, the magnitude of the predicted

Table 2. Model power 3-D at 25-s period normalized by $P_n^m(0)$.

m \ n	0	1	2	3	4	5	6	7	8
0	0.121	–	–	–	–	–	–	–	–
1	–	−0.102	–	–	–	–	–	–	–
2	0.115	–	0.076	–	–	–	–	–	–
3	–	0.068	–	−0.044	–	–	–	–	–
4	0.120	–	0.042	–	0.029	–	–	–	–
5	–	−0.065	–	0.025	–	−0.016	–	–	–
6	−0.081	–	0.042	–	−0.012	–	0.030	–	–
7	–	0.040	–	−0.007	–	0.006	–	−0.061	–
8	0.048	–	−0.013	–	0.019	–	−0.008	–	0.004

phase shift increases slightly (±0.01) but does not match the beamforming magnitude suggesting that differences in parameterization can lead to small but significant differences in phase prediction.

3.4 Predominantly 2-D (25-s period) versus 3-D (5-s period) source density models

In this section, we show the amplitude densities from the three-source density modelling methods examined in this study for a 25-s period, which has a strong 2-D source distribution and at 5 s, which has a 3-D component to the data. We chose to show these two periods because they exemplify the two end-member cases well for surface waves and body waves. These examples also provide a means of examining the efficacy of our three modelling approaches under different conditions.

Fig. 4(a) shows the equivalent 2-D density functions for the three methods at 25 s. The density functions are non-zero for all azimuths. The character of the three density functions are very similar, requiring a large peak in the sources at 290° azimuth. As expected the 2-D and 3-D models produce nearly identical distributions. The 2-D beamforming amplitude density function has a broader maximum peak with more energy at 250–270° azimuth, but is consistent with the other two models.

By comparing the variance reduction of the models versus the number of parameters required we can examine how quickly the three different models converge to an acceptable fit to the data so we can qualitatively assess the effectiveness of the three models. For 25-s period, the variance reduction between the three models is similar for large numbers of parameters, with maximum variance reductions of 67 per cent for the models shown in Fig. 3. Fig. 4(b) shows the variance reduction of the three models as a function of m for the 2-D model and n for the 3-D model relative to the 2-D BM which has 360 parameters. The 2-D BM has the same variance reduction at maximum resolution (120 resolved parameters) and at the resolution shown in Fig. 4(a) (17 resolved parameters). Unsurprisingly, the 2-D BM fits the data better than the zeroth-order/degree models. The 3-D model converges to within 2 per cent of the maximum variance reduction at $n = 6$ while the 2-D model converges at $m = 3$. At $m = n = 6$ where variance reduction becomes equivalent, the 3-D model requires 28 coefficients, relative to 13 coefficients needed to reach the same level of variance reduction for the 2-D model, suggesting the 2-D model is optimal. We present the synthetics in Figs 3(d–l) with $m = n = 8$ for the 2-D and 3-D models because the variance reduction of all three models is within <1 per cent for this number of coefficients.

The power in the model coefficients in the 2-D and 3-D models suggests that surfaces waves are dominant at 25-s period (Tables 1 and 2). The power of the coefficients for 25-s period for the 2-D model show that the $m = 0,1$ terms are the largest. To account for the several orders of magnitude increase in the value of $P_{\rm n}^{\rm m}(0)$ at high order and degree and to show the relative importance of the power of the coefficients to each other, we present the 3-D coefficients multiplied by $P_{\rm n}^{\rm m}(0)$. For the 3-D model, the $n = 0$ coefficient is significant but the same order of magnitude as some of the higher-order harmonics ($n = 2$, $m = 0$ and $n = 4$, $m = 0$), suggesting the NCF is not produced by a 3-D noise source density.

We examine the potential for 3-D noise source distributions at 25-s period by comparing the normalized beamformer output (Fig. 4c) to the 3-D model (Fig. 4d). The 3-D source density function plot (Fig. 4d) is dominated by the high amplitude densities at horizontal to nearly horizontal angles (90°) and near zero amplitude densities in the vertical directions. The 3-D density function is symmetric in the upper and lower hemispheres, so we show only the lower hemisphere. The beamformer output (Fig. 4c) shows a similar pattern, with high beamformer output at slownesses (∼0.27 s km^{-1}) corresponding to surface wave phase velocities, but the beamformer output is much smoother than the equivalent 2-D source densities shown in Fig. 4(a) highlighting the need to deconvolve the array response. It is interesting to note, that the increase in beamformer output at 0.1–0.2 s km^{-1} slowness and −60° to −30° azimuth, associated with body waves or vertically incident scattering also appears to be present in the 3-D source density model.

At 5 s, where the strongest signal is from waves arriving at high incidence angles, the 2-D nor the 3-D models adequately describe the data with maximum variance reductions of 15 and 19 per cent, respectively. In this period range the primary feature in the beamformer output are the peaks at slownesses <0.1 s km^{-1} (Fig. 5b). In the 3-D model (Fig. 5c) we have increased n in eq. 4 to 20 to better match the resolution of the beamformer output; the peaks are broadened due to the truncation of the series but have good agreement. The low horizontal slowness of the waves could be body waves generated by the microseism (e.g. Gerstoft *et al.* 2008), or scattered surface waves. We prefer the former explanation because of the correlation of backprojected location of these phases with significant wave height models, but we cannot conclusively rule out the later possibility. There is some surface wave energy visible in the beamformer output and Fig. 5(a) shows the equivalent 2-D source density function for the three models. The 2-D model and 3-D model have significant surface wave energy and are in general agreement with each other and the small peak observed in the beamformer 2-D model (Fig. 5a). The influence of body waves causes the 2-D model to breakdown and therefore eq. (3) or (4) with a more realistic body wave velocity model must be used to invert for the 3-D source density function.

4 DISCUSSION

4.1 Source density dimensionality

At longer periods (>7 s), all three models recover noise source density functions that are dominated by surface waves. This is consistent with previous studies that have shown that the sources in ambient noise are surface waves generated by ocean wave derived sources (Rhie &

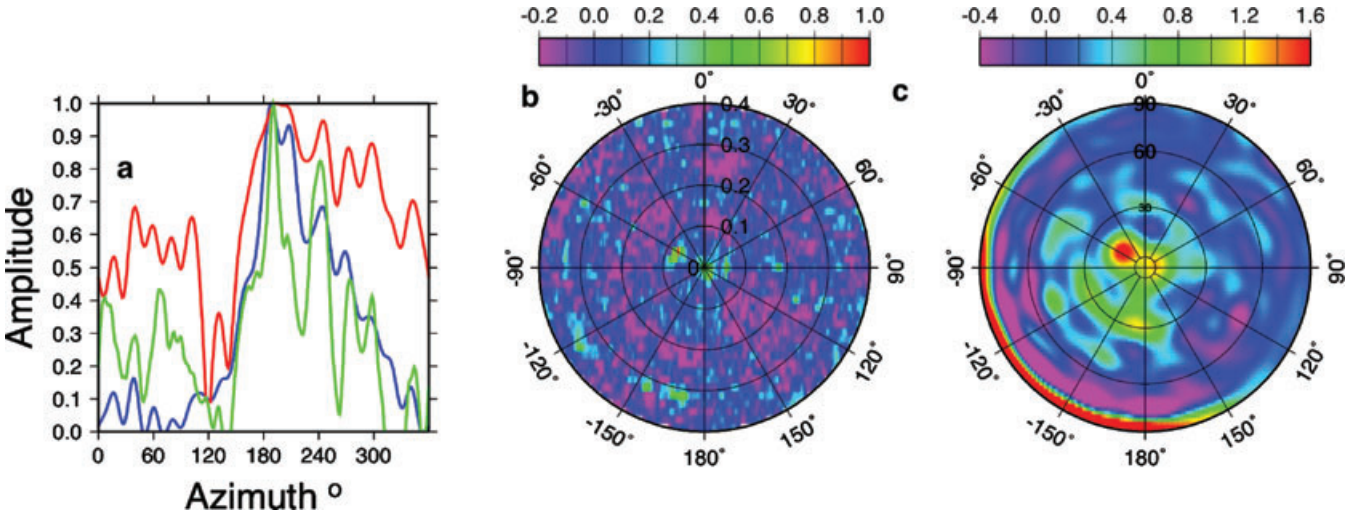

Figure 5. Comparison of the three methods at 5-s period. (a) 2-D (blue), 3-D (red) and 2-D beamformer (green) equivalent 2-D models. (b) beamformer output azimuth versus slowness and (c) 3-D model density function azimuth versus incidence angle.

Romanowicz 2006; Stehly *et al.* 2006; Tanimoto 2007; Yang & Ritzwoller 2008; Webb 2008). Both the 3-D model and beamformer output show little energy coming from body waves (Figs 4c and d), so for ambient noise studies, a 2-D model is sufficient for characterizing the noise field in this period range.

At short periods, there does appear to be a significant body wave signal. As shown at 5 s in Fig. 5, the 2-D models cannot cope with the body wave signals effectively due to the violation of the 2-D assumption. For detection of vertically incident noise sources, the beamforming method and the 3-D method provide the good resolution and are in reasonable agreement with each other. However, to recover accurate amplitude density information, an assumption about the velocity structure must be made to convert from slowness to incidence angle.

4.2 Predicted phase shifts

At long periods, the 2-D, 3-D and beamforming methods predict similar surface wave source density functions, with similar fits to the data, but the 3-D model does not match the observed phase shift well. The 3-D model has a significant sinc function component and it matches observed amplitudes well, but there is a substantial phase shift between the 2-D and 3-D models for >3 distance/wavelength or cycles (Figs 3f and i). This phase shift is not observed in the data (Fig. 3c), which has an average of $\sim$0.125 cycles for wavenumbers <4. The apparent error in the phase shift of the 3-D model, likely reflects errors introduced by truncation of the series for the 3-D model and the loss of the odd terms due to the station geometry. This suggests that the 2-D models and 2-D BM are better for characterizing the source density function and predicting phase shifts at longer periods.

The azimuthal pattern between the 2-D and 2-D BM predicted phase shift is similar but there is a difference in the magnitude. Some of the differences in the magnitude of the predicted phase shift between the 2-D and 2-D BM (Figs 3f and l) may be due to earth structure and scattering. The 2-D model accounts for Earth structure somewhat by taking the average phase velocity between station pairs, but as discussed by Tsai (2009) and Yao & van der Hilst (2009), Earth structure outside the station-to-station path may also introduce small phase delays. There may be some error in the 2-D model estimate of the required phase shift presented. An iterative approach with complete regional velocity tomography to readjust the phase velocity at each iteration could help (Yao & van der Hilst 2009). On the other hand, the beamforming model assumes an average velocity across the array. Averaging over slowness in the beamformer output should help to reduce the effects of heterogeneity somewhat. The small ($<$1 per cent) difference in variance reduction between the 2-D model and the 2-D BM suggests the long wavelength source density function may be sufficient for characterizing the phase shifts in the data due to source effects. We prefer the 2-D model for long periods because it requires the least number of parameters and has a more accurate velocity model, which gives the most conservative estimate for δ.

4.3 Effects of inhomogeneous source density on isotropic and anisotropic phase velocity

The source density function from all three methods is inhomogeneous and produces an azimuthal trend in the phase shift of the symmetric FNCF. This will map into an azimuthal trend in phase velocity at a given distance/wavelength if the phase is only corrected for an isotropic source density function. For a mostly 2-D source distribution, the phase shift and phase velocity for symmetric component of the NCF has sinusoidal 2θ and 4θ azimuthal dependence from eq. 10. This is the same expected variation for azimuthal anisotropy if we assume Rayleigh wave azimuthal anisotropy of the form $c_0 + c_1\cos(2\theta\text{-}\psi_1) + c_2\cos(4\theta\text{-}\psi_2)$ after Smith & Dahlen (1973) where c_0 is the isotropic phase velocity, c_1 and c_2 are the anisotropic contributions to the phase velocity and ψ_1 and ψ_2 are the fast azimuth directions. Therefore, source inhomogeneity could be mapped into estimates of azimuthal anisotropy.

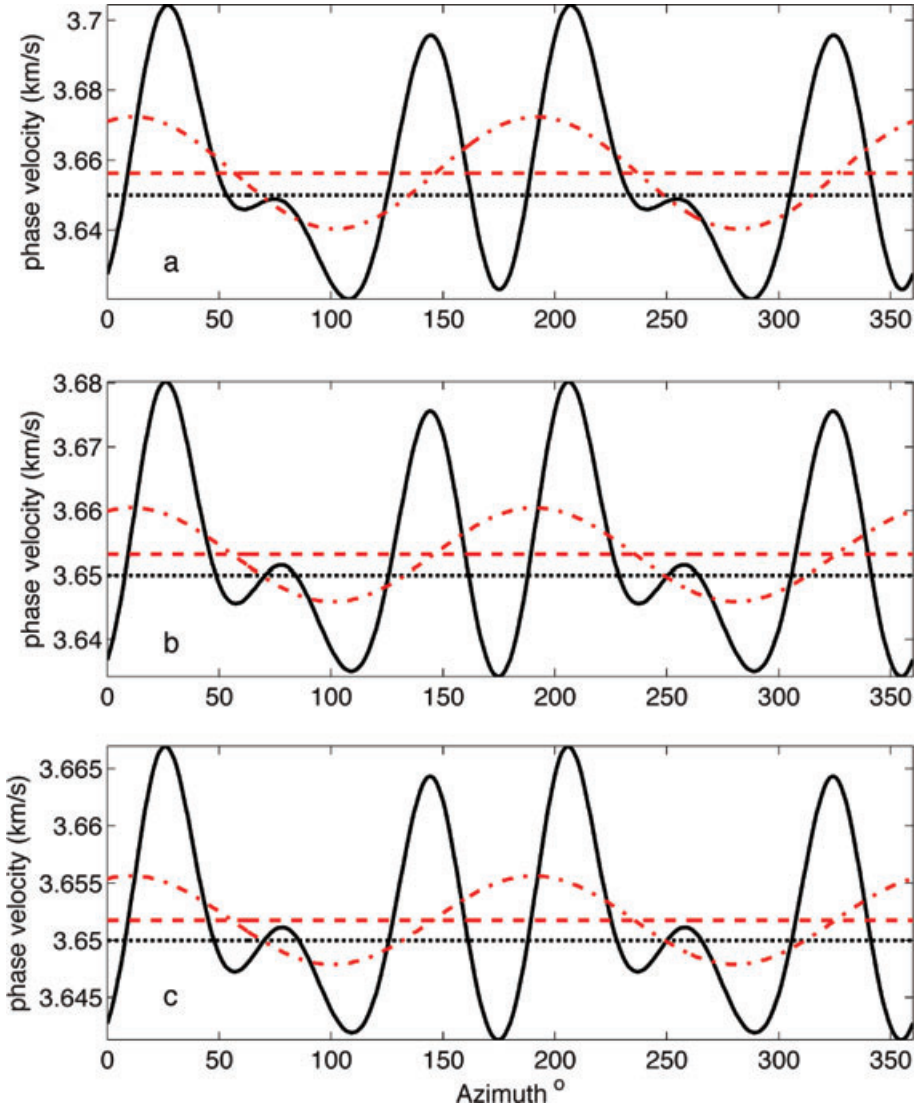

Figure 6. Synthetic FNCF phase shift at 25-s period (Fig. 3f) mapped into apparent phase velocity (black line) due to inhomogeneous source at (a) 2, (b) 3 and (c) 4 distance/wavelength. The true phase velocity used for the calculation of the synthetics is shown as the dotted grid line at 3.65 km s^{-1}. Dashed red grid line shows the isotropic velocity (c_0) predicted from the phase velocity at those regions and the dashed-dotted red line shows the best-fitting 2θ anisotropy model [$c_0 + c_1\cos(2\theta - \psi_1)$].

We illustrate the potential effects of inhomogeneous source on phase velocity estimates by mapping the synthetic phase shift, $\delta + \pi/4$, in Fig. 3(f) to phase velocity. We then solve for c_0, c_1 and ψ_1 at a given distance/wavelength in the Smith & Dahlen (1973) model, ignoring the 4θ terms. We plot our results in Fig. 6 a, b, c for 2, 3, and 4 distance/wavelength, respectively. The phase is calculated using the symmetric component, so the phase velocity curves repeat every 180° of azimuth because they have an inherent 2θ, 4θ, 6θ and 8θ variation due to the even terms in eq. (10).

For a 1-D isotropic phase velocity study which solves only for c_0, the azimuthal variation in phase shift observed in Fig. 3(f) at 25-s period would be averaged, resulting in an isotropic mean phase velocity that is 0.1 to 0.2 per cent higher than the true phase velocity (3.65 km s^{-1}) going from 4 to 2 cycles or distance/wavelength. This increased velocity results from an average phase shift of −0.128 cycles, which is a direct result of both the asymptotic behaviour of the phase of J_0 at low distance/wavelength and the inhomogeneous source density. We observe this negative bias when averaging over our large and well-distributed station distribution in southern California. In addition, we also caution that the results from linear arrays can also be biased in both a positive and negative sense, for example if the stations happened to be aligned on the blue streaks in Fig. 3(f) the estimated velocity would be faster than the true velocity and the estimated velocity from stations aligned on any green portion, for example, N–S or W–E, would be slower than the true velocity.

If the observed range of phase difference in Fig. 3(f) for 25-s period is mapped into azimuthal variation of phase velocity, the −0.02 to 0.01 cycles phase difference from the isotropically distributed noise translates to a peak-to-peak variation of phase velocity of 1 per cent down to 0 per cent from 2–4 distance/wavelength or cycles. In this particular example, the variation has a strong 2θ periodicity (note the large coefficient in Table 1 at $m = 2$), which could lead to a spurious apparent azimuthal anisotropy. Most of the data at 25-s period lie within 2–4

distance/wavelength. In particular, at 2 distance/wavelength we find peak-to-peak anisotropy of 1 per cent. This percentage is of the same order of the strength of anisotropy determined by other methods in this region, for example, 4 per cent from SKS splitting which integrates shear wave anisotropy over the entire mantle (Liu *et al.* 1995) and 1–2 per cent peak to peak anisotropy from teleseismic surface waves (Yang & Forsyth 2006).

The spurious effect of inhomogeneous noise source distribution on azimuthal anisotropy estimates only occurs for station pair distances $<$ $3\times$ wavelength. In this synthetic example, to minimize error in azimuthal anisotropy estimates without explicitly accounting for source effects, only station-to-station pairs whose distances are greater than $3\times$ the wavelength should be used, which is in keeping with current practices. Although it is also possible for the Earth's anisotropic structure to map into source heterogeneity, full anisotropic velocity tomography can be used in conjunction with source solutions to fully solve this problem (Yao & van der Hilst 2009).

4.4 Effect of inhomogeneous source density on 1-D attenuation estimates

The amplitude of seismic signals depends on the distance from the source (geometric spreading), the source, scattering and focusing effects caused by velocity heterogeneity and intrinsic attenuation of the Earth. To extract information about the Earth's intrinsic attenuation from ambient noise studies, the effects of velocity heterogeneity, geometric spreading and source should be accounted for. The 2-D model presented here provides a means of addressing the source and geometric spreading effects. Here we will illustrate the potential uncertainty in attenuation measurements caused by assuming an isotropic noise source distribution using synthetic, attenuation-free data generated by inhomogeneous source distributions modelled from our southern California data.

The azimuthal variation of amplitude poses a problem for attenuation studies because uneven sampling across azimuths could lead to a biased 1-D estimate of amplitude versus distance. Specifically, as we show for 25-s period in Fig. 3(a), the station geometry used in this study preferentially samples NW trends, which is also roughly parallel to where the strongest gradients in the real component of the FNCF with azimuth occur. If estimates of 1-D attenuation were made using station pairs in a narrow azimuth range some of the source effects would be mitigated; however, this would severely limit the number of observations. On the other hand, forming a 1-D attenuation estimate by sampling the real component of the FNCF over a broader range of azimuths across the azimuthal gradient in the FNCF would cause a 1-D variation with distance in amplitude not due to simple geometric spreading. Therefore, modelling this variation assuming a homogenous source distribution and assuming the zero-order 2-D model with $1/\sqrt{s}$ geometric spreading, could lead to spurious estimates of intrinsic attenuation.

To estimate and illustrate the possible error due to sampling bias of the azimuthal variation and the assumption of an isotropic source density, we use the real component of the synthetic FNCF from our best-fit 2-D model at 7.5, 15, 20 and 25-s period, where $m = 8$ and c is the empirically determined phase velocity from Section 2.5 for each station-to-station pair. Again, the synthetic data are free of intrinsic attenuation. We estimate the attenuation coefficient, α, using a modified model of FNCF attenuation of Prieto *et al.* (2009) of the form:

$$R(\omega, s/c(\omega), \alpha) = A(\omega) J_0\left(\frac{\omega s}{c(\omega)}\right) \exp(-\alpha s), \tag{12}$$

where A is amplitude. We solve for A and α using a grid search fitting the synthetic data. We present the best-fitting positive α as our best estimate of the potential uncertainty with 95 per cent confidence regions shown in Fig. 7.

From azimuthal variation and an assumed isotropic source density we estimate the total range of best-fitting α to be 0.2–1.1 $\times$ 10^{-3} km^{-1} (Fig. 7). At 20-s period $\alpha = 0.3 \times 10^{-3}$ km^{-1} and at 15-s period $\alpha = 1.1 \times 10^{-3}$ km^{-1}, which are significant from zero. At 25-s period α $= 0.2 \times 10^{-3}$ km^{-1} and at 7.5 s, which has a nearly time invariant coastal noise source from the microseism, $\alpha = 0.5 \times 10^{-3}$ km^{-1}, although

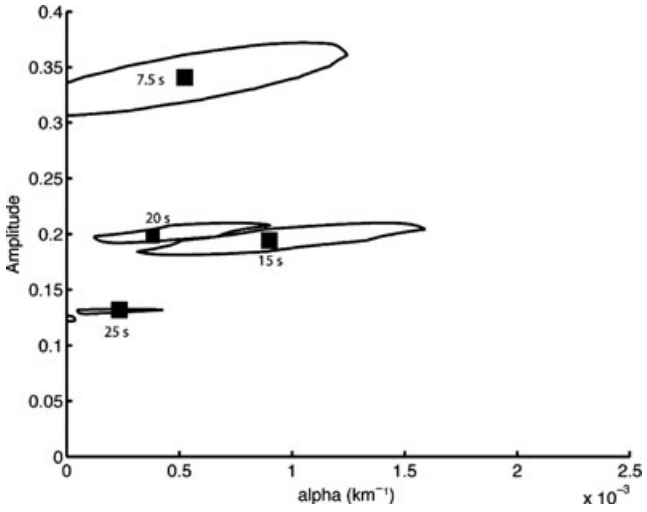

Figure 7. Grid search results for 1-D synthetic FNCF attenuation. Blacks squares indicate best-fitting α and A for period shown in label. Black line around squares indicate 95 per cent confidence regions.

these are not significant from zero. However, we note that these values are the same order of magnitude as observed in Prieto *et al.* (2009) (0.27–6.4 $\times$ 10^{-3} km^{-1} from 25–5-s period); the larger values correspond to shorter periods. Our estimates are from a different time period of noise; however, temporal variation in the general pattern of sources is unlikely to be much different for the region (e.g. the consistency between this study and Stehly *et al.* 2006; Yang & Ritzwoller 2008). Therefore, our results suggest that the uncertainty in the attenuation measurements are larger and may have a stronger frequency dependence than those presented in a previous study (Prieto *et al.* 2009).

Source effects, focusing, instability in the inversion process, or source distribution could cause negative α or amplitude increase with distance. We only consider positive values for α, but some of the confidence regions overlap negative α and there may be some periods where the global minimum lies completely within negative α space. We have a homogenous velocity structure and no variation in radiation pattern of our sources; therefore, the overlap with negative α represents the effect of inhomogeneous source distributions. In real data, without consideration of the source distribution, negative α could be erroneously interpreted as focusing, a source effect or an unstable inversion in real data.

To mitigate the effects of source distribution on ambient noise attenuation studies, higher order 2-D models might be necessary. In addition, we think the effects of scattering and focusing may need to be accounted for especially at short periods, which are sensitive to shallow structure where strong velocity gradients may exist.

5 CONCLUSIONS

We investigated the effects of noise source distribution on 1-D isotropic and anisotropic phase velocity estimates and attenuation estimates. We determined the dimensionality and heterogeneity of noise source distributions in southern California by inverting the FNCF for 2-D and 3-D source density functions using a 2-D plane wave model, a 3-D plane wave model and beamforming. We find evidence for both 2-D and 3-D source distributions at different period ranges. At long periods (>7 s) the noise field is effectively 2-D, therefore we prefer the 2-D plane wave model because it requires the fewest number of parameters to achieve the same maximum variance reduction out of the three methods tested. At short periods (<7 s) the noise field has a body wave component, which can only be resolved by the 3-D and beamforming models. For all periods the source density is not homogenous in southern California, indicating that estimates of phase velocity from the NCF will have a bias due to source effects and the amplitude of the FNCF will have an azimuthal dependence. We provide analytical means to correct the apparent station-to-station NCF phase for inhomogeneous source distributions to improve the accuracy of phase velocity tomographic inversions. From synthetic NCF we quantify the potential biases in estimates of anisotropy and attenuation that arise from assuming an isotropic noise source density for NCF derived from an inhomogeneous density. Specifically, we estimate the bias in the isotropic phase velocity in southern California will be about 0.0–0.2 per cent faster at 25 s, which is probably within the error of isotropic phase velocity estimates. The noise source distribution southern California can cause an apparent aziumuthal anisotropy in phase velocity up to 1 per cent. Similarly, azimuthal changes in amplitude could be mapped into artificial attenuation yielding attenuation coefficients up to 1.1 $\times$ 10^{-3} km^{-1} at 15-s period. These error estimates illustrate the potential dangers of not accounting for inhomogeneous noise sources in ambient noise studies and therefore we recommend that source density analysis be performed to mitigate and correct these biases.

ACKNOWLEDGMENTS

We would like to thank the editor, David Halliday, Victor Tsai, Kasper Van Wijk and one anonymous reviewer for helpful and constructive comments.

REFERENCES

Aki, K., 1957. Space and time spectra of stationary and stochastic waves, with special reference to microtremors, *Bull. Earthq. Res. Inst.,* **35,** 415–457.

Aki, K. & Richards, P.G., 2002. *Quantitative Seismology,* University Science Books, Sausalito, California.

Bendat, J.S. & Piersol, A.G., 2000. *Random Data Analysis and Measurment Procedures,* 3rd edn, Wiley and Sons, New York.

Bensen, G.D., Ritzwoller, M.H., Barmin, M.P., Levshin, A.L., Lin, F., Moschetti, M.P., Shapiro, N.M. & Yang, Y., 2007. Processing seismic ambient noise data to obtain reliable broad-band surface wave dispersion measurements, *Geophys. J. Int.,* **169,** doi:10.1111/j.1365-1246X.2007.03374.x.

Cox, H., 1973. Spatial correlation in arbitrary noise fields with application to ambient sea noise, *J. acoust. Soc. Am.,* **54,** 1289–1301.

Cupillard, P. & Capdeville, Y., 2010. On the amplitude of surface waves obtained by noise correlation and the capability to recover the attenuation: a numerical approach, *Geophys. J. Int.,* **181,** 1687–1700, doi:10.1111/j.1365-1246X.2010.04586.x.

Cupillard, P., Capdeville, Y. & Stehly, L., 2008. Recovering the attenuation of surface waves from noise correlation : synthetic tests in a spherically symmetric Earth, *Eos, Trans. Am. geophys. Un.,* **89,** Fall Meeting Suppl. S31A-1895.

Ekström, G., Abers, G.A. & Webb, S.C., 2009. Determination of surface-wave phase velocities across USArray from noise and Aki's spectral formulation, *Geophys. Res. Lett.,* **36,** L18301, doi:18310.11029/12009GL039131.

Gerstoft, P., Shearer, P., Harmon, N. & Zhang, J., 2008. Global P,PP, and PKP wave microseisms observed from distant storms, *Geophys. Res. Lett.,* **35,** L23306, doi:23310.21029/22008GL036111.

Gerstoft, P. & Tanimoto, T., 2007. A year of microseisms in southern California, *Geophys. Res. Lett.,* **34,** L20304, doi:20310.21029/22007GL031091.

Halliday, D. & Curtis, A., 2008. Seismic interferometry, surface waves and source distribution, *Geophys. J. Int.,* **175,** 1067–1087.

Harmon, N., Forsyth, D. & Webb, S., 2007. Using ambient seismic noise to determine short-period phase velocities and shallow shear velocities in young oceanic Lithosphere, *Bull. Seis. Soc. Am.,* **97,** 2024–2039.

Harmon, N., Gerstoft, P., Rychert, C.A., Abers, G.A., Salas de la Cruz, M. & Fischer, K.M., 2008. Phase velocities from seismic noise using beamforming and cross correlation in Costa Rica and Nicaragua, *Geophys. Res. Lett.,* **35,** doi:10.1029/2008GL03587.

Lin, F., Moschetti, M.P. & Ritzwoller, M.H., 2008. Surface wave tomography of the western United States from ambient seismic noise: Rayleigh and Love wave phase velocity maps, *Geophys. J. Int.,* **173,** 281–298, doi:10.1111/j1365-1246X.2008.03720.x.

Liu, H., Davis, P.M. & Gao, S., 1995. SKS splitting beneath southern California, *Geophys. Res. Lett.,* **22,** 767–770.

Matzel, E., 2008. Attenuation tomography using ambient noise correlation, *Seism. Res. Lett.,* **79,** 358.

Nakahara, H., 2006. A systematic study of theoretical relations between spatial correlation and Green's function in one-,two-,and three-dimensional random scalar wavefields, *Geophys. J. Int.,* **167,** 1097–1105.

Oppenheim, A.V. & Schafer, R.W., 1975. *Digital Signal Processing,* Prentice-Hall, Inc, Englewood Cliffs, New Jersey.

Prieto, G.A., Lawrence, J.F. & Beroza, G.C., 2009. Anelastic Earth structure from the coherency of the ambient seismic field, *J. Geophys. Res.,* **114,** doi:10.1029/2008JB0006067.

Rhie, J. & Romanowicz, B., 2006. A study of the relation between ocean storms and the earth's hum, *Geochem. Geophys. Geosyst.,* **7,** doi:10.1029/2006GC001274.

Sabra, K.G., Gerstoft, P., Roux, P., Kuperman, W.A. & Fehler, M.C., 2005. Surface wave tomography from microseisms in Southern California, *Geophys. Res. Lett.,* **32,** doi:10.1029/2005GL023155.

Sanchez-Sesma, F.J. & Campillo, M., 2006. Retrieval of the green's function from cross correlation: the canonical elastic problem, *Bull. Seis. Soc. Am.,* **96,** 1182–1191.

Shapiro, N.M., Campillo, M., Stehly, L. & Ritzwoller, M.H., 2005. High-resolution surface-wave tomography from ambient seismic noise, *Science,* **307,** 1615–1618.

Smith, M.L. & Dahlen, F.A., 1973. Azimuthal Dependence of Love and Rayleigh-Wave Propagation in a Slightly Anisotropic Medium, *J. geophys. Res.,* **78,** 3321–3333.

Snieder, R., 2004. Extracting the Green's function from the correlation of coda wave: a derivation based on stationary phase, *Phys. Rev. C,* **69,** doi:10.1103/PhysRevE.1169.046610.

Stehly, L., Campillo, M. & Shapiro, N.M., 2006. A study of seismic noise from its long range correlation properties, *J. geophys. Res.,* **111,** B10206, doi:10210.11029/12005JB004237.

Tanimoto, T., 2007. Excitation of microseisms, *Geophys. Res. Lett.,* **34,** L05308, doi:05310.01029/02006GL029046.

Tsai, V.C., 2009. On establishing the accuracy of noise tomography travel-time measurements in a realistic medium, *Geophys. J. Int.,* **178,** 1555–1564.

Webb, S.C., 2008. The Earth's Hum: the excitation of Earth normal modes by ocean waves, *Geophys. J. Int.,* **174,** 542–566.

Westwood, E.K., 1992. Broadband matched-field source localization, *J. acoust. Soc. Am.,* **91,** 2777–2789.

Yang, Y. & Forsyth, D.W., 2006. Rayleigh wave phase velocities, small-scale convection, and azimuthal anisotropy beneath southern California, *J. geophys. Res.,* **111,** B07306, doi:07310.01029/02005JB004180.

Yang, Y. & Ritzwoller, M.H., 2008. The characteristics of ambient seismic noise as a source for surface wave tomography, *Geochem., Geophys., Geosys.,* **9,** Q02008, doi:02010.01029/02007GC001814.

Yang, Y., Ritzwoller, M.H., Lin, F.C., Moschetti, M.P. & Shapiro, N.M., 2008. The structure of the crust and uppermost mantle beneath the western US revealed by ambient noise and earthquake tomography, *J. geophys. Res.,* **113,** B12310, doi:12310.11029/12008JB005833.

Yao, H. & van der Hilst, R., 2009. Analysis of ambient noise energy distribution and phase velocity bias in ambient noise tomography, with application to SE Tibet, *Geophys. J. Int.,* **179,** doi:10.1111/j.1365-1246X.2009.04329.x.

Yao, H., van der Hilst, R.D. & De Hoop, M.V., 2006. Surface-wave array tomography in SE Tibet from ambient seismic noise and two-station analysis: I–Phase velocity maps, *Geophys. J. Int.,* **166,** 732–744, doi:710.1111/j.1365-1246X.2006.03028.x.

Yardibi, T., Li, J., Stoica, P. & Cattafesta, L.N., 2008. Sparsity constrained deconvolution approaches for acoustic source mapping, *J. acoust. Soc. Am.,* **123,** 2631–2642.